Enhanced performance of ultraviolet AlGaN/GaN photo-HEMTs by optimized channel isolation schemes

Ramit Kumar Mondal, Zhongshu Xiong, Mohan Kumar Ghimire, Ravikiran Lingaparthi, Dharmarasu Nethaji, K Radhakrishnan, and Munho Kim*

School of Electrical and Electronic Engineering, Nanyang Technological University, 50 Nanyang Avenue, Singapore 639798

*Author to whom correspondence should be addressed. Email: munho.kim@ntu.edu.sg

KEYWORDS: MIS; Photo-HEMT; AlGaN/GaN; UV photodetector

Abstract

Solar blind ultraviolet (UV) photodetectors utilizing AlGaN/GaN high electron mobility transistor (HEMT) structure offer a very high responsivity, photo to dark current ratio (PDCR) and detectivity. However, the performance of conventional mesa isolated photo-HEMT is limited due to current leakage paths through the side wall and AlGaN barrier. In this work, apart from conventional mesa type isolation, ion implantation and metal-insulator-semiconductor (MIS) schemes have been adopted to isolate the channels of AlGaN/GaN photo-HEMTs. We achieve a significant reduction in dark current for MIS photo-HEMT of around four and three orders of magnitude as compared to those of conventional mesa and ion implanted photo-HEMTs, respectively. Moreover, the responsivity and PDCR of MIS photo-HEMT are around three and four orders of magnitude higher than those of conventional mesa isolated photo-HEMT. Subsequently, MIS photo-HEMT on Si substrate has achieved a very high detectivity of 4.63×10^{16} Jones at the UV incidence wavelength of 360 nm. The results presented in this work establish the advantages of MIS photo-HEMT over other types of photo-HEMTs. In addition, compatibility with GaN device fabrication technology and significantly enhanced optoelectronic performance suggest AlGaN/GaN MIS photo-HEMTs as a promising candidate for a variety of advanced UV sensing applications.

Introduction

In recent years, GaN technology has matured enough to replace Si based technology for certain applications such as high-power electronics and ultraviolet (UV) optoelectronics [1,2]. Nitride based semiconductors have several benefits over other semiconductor materials due to their wide bandgap tunability, inherently high temperature and radiation tolerance and superior durability [3]. With these benefits, GaN has been enormously used to develop various devices such as light emitting diodes (LEDs), high electron mobility transistors (HEMTs) and photodetectors (PDs). A direct bandgap of 3.42 eV makes GaN an ideal material for visible blind UV detection, which is suitable for many diverse applications such as combustion flame detection, UV astronomy, satellite positioning etc. [4–6].

Many research groups worldwide have developed various types of GaN UV PDs based on GaN/Ga_2O_3 [7,8], GaN/MoO_{3-x} [9], GaN/ZnO heterostructures [10], GaN/Ag nanowires[11] etc. Among various device structures, two-dimensional electron gas (2DEG) at the AlGaN/GaN HEMT has enabled a significant revolution in the development of the high frequency power transistor [12] and highly responsive UV PDs [13,14]. Specifically, 2DEG AlGaN/GaN PDs outperform other types of GaN PDs based on p-i-n [15], Schottky barrier [16], avalanche [17], field effect transistor [18], fin shaped capacitor [19] and metal−semiconductor−metal (MSM) structure [20][21]. In addition, the fabrication process of AlGaN/GaN 2DEG PDs is well compatible with the matured GaN fabrication technology.

However, although the presence of spontaneously formed 2DEG has produced a very high responsivity (R) exceeding 10^9 A/W, it also resulted in high dark current in the same order as of photocurrent [22]. Thus, it is difficult to achieve accurate and reliable detection of UV light. The 2DEG is disconnected to reduce dark current considerably. There are a few approaches to disconnect the inherently formed 2DEG channel at the AlGaN/GaN interface. First, the 2DEG channel was disconnected via the physical etching of AlGaN region, leading to recess gate configuration [23]. Second, the 2DEG channels were disconnected using band-engineered structures such as p-GaN gate on top of AlGaN/GaN [24,25] or AlGaN/n-GaN/p-GaN heterostructure [26]. Third, the 2DEG can be depleted by applying a negative bias at the gate electrode, lower than the threshold voltage of the HEMT [27]. When a negative voltage below the threshold voltage of HEMT is applied at the gate, the 2DEG channel region below the gate electrode is depleted of electrons. This is called the off-state operation of HEMT. The drain to source current becomes very nominal under this condition, driving the HEMT into off-state condition. The HEMT should be operated under off-state condition for a reliable and faithful photodetection. The first and second types of PDs are two terminal devices. Conversely, the third type of PD is essentially a three terminal device comprising of source, drain and gate electrodes. Apart from comparatively higher photoresponsivity than the two terminal PDs, the three terminal phototransistor is adaptable to advanced functionalities such as optoelectronic signal mixing[28] and active pixel imaging [29]. It is notable that two terminal PDs cannot support these functionalities.

It is expected that the effective channel isolation of HEMTs will enhance the device performance by suppressing the leakage current. The conventional method to isolate the channel is the etched mesa structure. However, it causes large leakage current which makes it challenging to detect the weak UV light. It was recently reported that ion implantation [30] or metal-insulator-semiconductor (MIS) [31] structure provides superior isolation of the channel in HEMTs to alleviate leakage current. Till now, the mesa structure has been the only way to isolate the gate electrode pad and the 2DEG channel in photo-HEMTs [32,33]. The adaptation of MIS or ion-implantation route has not been reported for photo-HEMT yet.

In this article, we have developed ion-implantation and MIS schemes to isolate the channel region of AlGaN/GaN photo-HEMTs on Si substrates. Owing to the reduced leakage path, the ion implanted and

MIS photo-HEMTs offer remarkably low dark current as well as large photocurrent compared to the MESA photo-HEMTs. An analytical comparison among three types of photo-HEMTs (*i.e.*, Mesa, Ion-implanted, and MIS) has been carried out to present the superiority of MIS photo-HEMTs over other two isolation schemes. Our results show that the MIS structure can be a viable approach to form an effective channel isolation of the photo-HEMT that enables a high-performance UV sensing capability.

Result and Discussion

Characterization of HEMT epi-structure on Si substrate

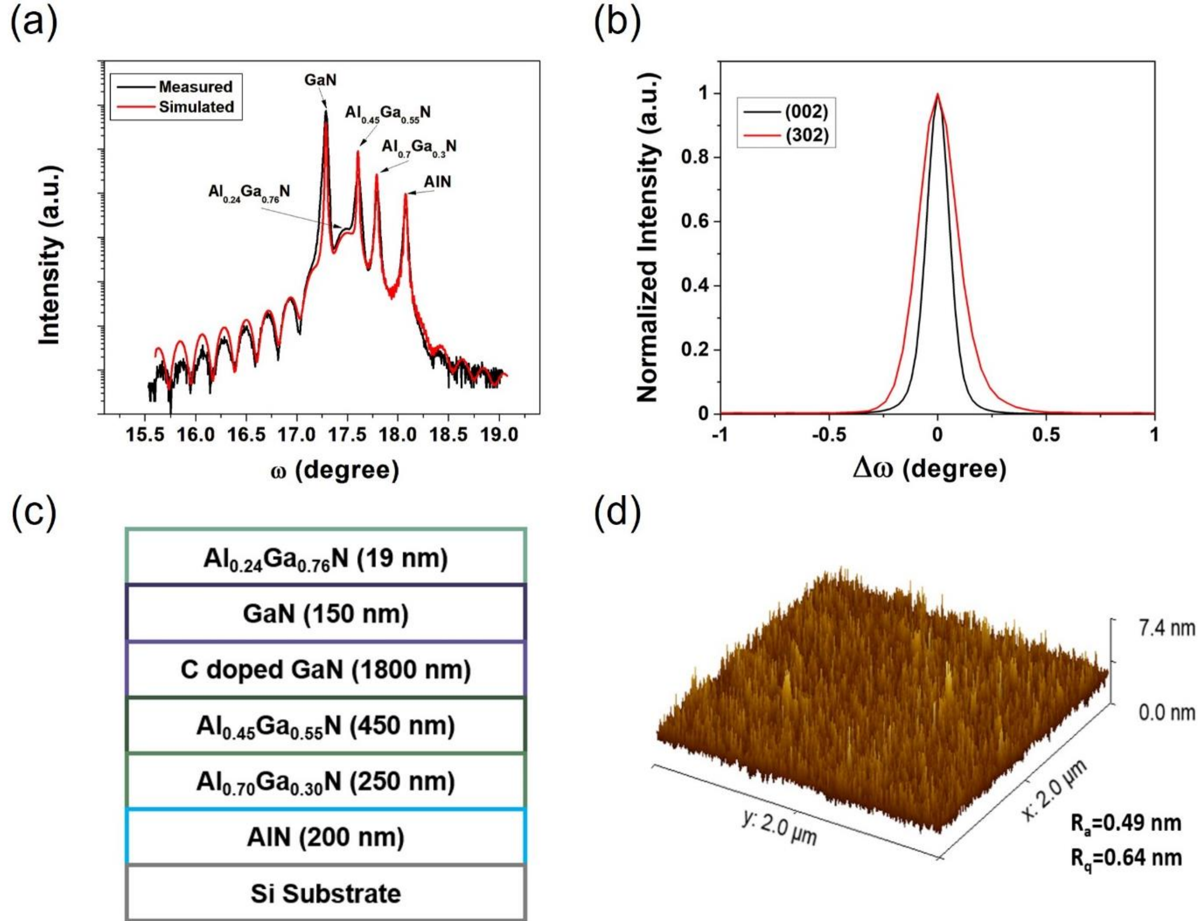

Fig 1. Characterization of HEMT epi-structure on Si substrates: (a) HRXRD ω-2θ scan along GaN (002) and (b) HRXRD rocking curve scans along GaN (002) and (302) (c) Cross-sectional schematic of the epi-structure (d) AFM image of the AlGaN/GaN surface.

HEMT epi-structure of undoped AlGaN barrier (19 nm)/ GaN channel (150 nm) was grown on Si substrates using metal-organic chemical vapor deposition (MOCVD) technique. Several material characterization methods were used to investigate the microstructural properties of the epi-structure. **Fig 1(a)** and **1(b)** exhibit the X-ray diffraction (XRD) ω-2θ scan along GaN (002) and rocking curve along GaN (002) and GaN (302), respectively. The experimental spectrum of ω-2θ scan was fitted to extract the AlGaN barrier composition of 24% (**Fig 1(a)**). Strong pendullÖsung fringes in the ω-2θ scan indicate good structural perfection and abrupt interfaces of heterostructure along the c-direction. HRXRD reveals peaks at 17.28°, 17.50°, 17.61°, 17.50°, 17.79° and 18.07° which correspond to the (002) GaN, $Al_{0.24}Ga_{0.76}N$, $Al_{0.45}Ga_{0.55}N$, $Al_{0.70}Ga_{0.30}N$ and AlN, respectively. The full widths half maximum (FWHM) of the XRD rocking curve along symmetric (002) and skew-symmetric (302) were used to estimate the

screw and edge-dislocation density, respectively [34]. The screw and edge-dislocation densities were estimated to be 3.44×10^9 and 4.54×10^8 /cm^2, respectively. The values are comparable to those of other HEMT structures on Si. The cross-sectional schematic of the HEMT epi-structure (**Fig 1(c)**) reveals the thicknesses of each layer along with material composition on Si substrate. **Fig S1** shows the cross-sectional structure of the wafer. The surface roughness of the film was evaluated by atomic force microscopy (AFM), carried out on an area of 2×2 μm^2 (**Fig 1(d)**). The average (R_a) and root mean square (R_q) surface roughness were measured to be 0.49 and 0.64 nm, respectively. The values for 2DEG concentration, 2DEG mobility, sheet resistance and uniformity were 9×10^{12}/ cm^2, 1500 cm^2/ V.s, 350 Ω/sq, and < 5%, respectively.

Channel isolation schemes

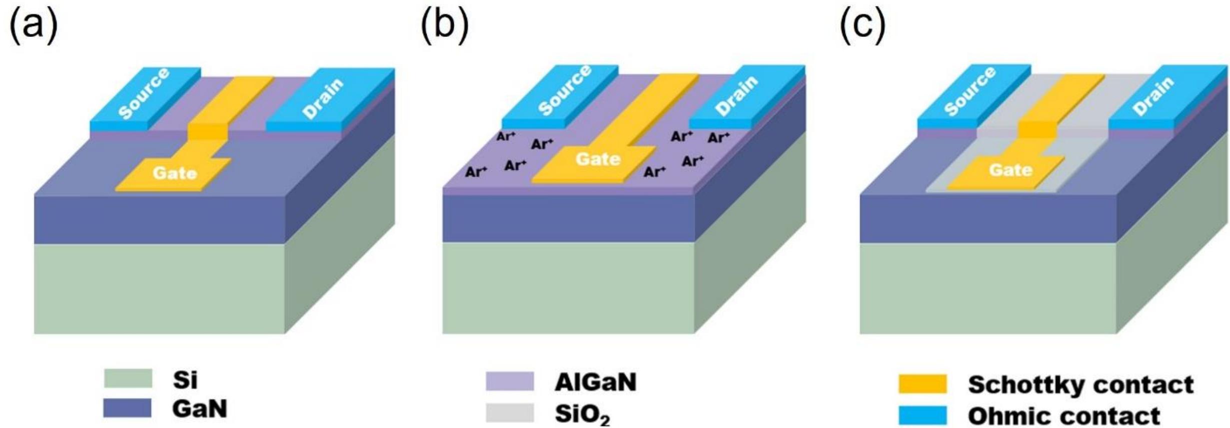

Fig 2. Schematic cross-sectional structures: (a) MESA, (b) ION, and (c) MIS photo-HEMTs.

The above channel isolation schemes were employed to develop three different types of photo-HEMTs. In first type of photo-HEMT (*i.e.*, MESA photo-HEMT), gate isolation was achieved in the form of mesa structure by implementing Cl_2 based inductively coupled plasma (ICP) etching. In the second type of photo-HEMT (*i.e.*, Ion-implanted (ION) photo-HEMT), Ar^+ ions were implanted to diminish 2DEG to isolate the channel region instead of forming the mesa structure. Third type of photo-HEMT (*i.e.*, MIS photo-HEMT) was based on a 20 nm SiO_2 layer, deposited between gate electrode and AlGaN/GaN to make the MIS structure, serving the isolation purpose. **Fig 2** shows the 3D schematic cross-sectional structures of MESA, ION, and MIS photo-HEMTs. The optical microscopic images of the fabricated devices can be found in **Fig S2**. The gate length and width of the fabricated photo-HEMTs are 5 and 20 μm, respectively, leading to an UV absorption area of 100 μm^2. To maintain the transparency of gate electrode, we used a very thin layer of Ni/Au (5/5 nm) for all three configurations. This thin gate can maintain a transmittance of around 43 ~ 47% within our desired UV wavelength range (**Fig S3**). It is notable that 20 nm SiO_2 layer which covers the channel region of MIS photo-HEMT does not cause absorption loss (**Fig S3**).

Optoelectronic performance of photo-HEMTs

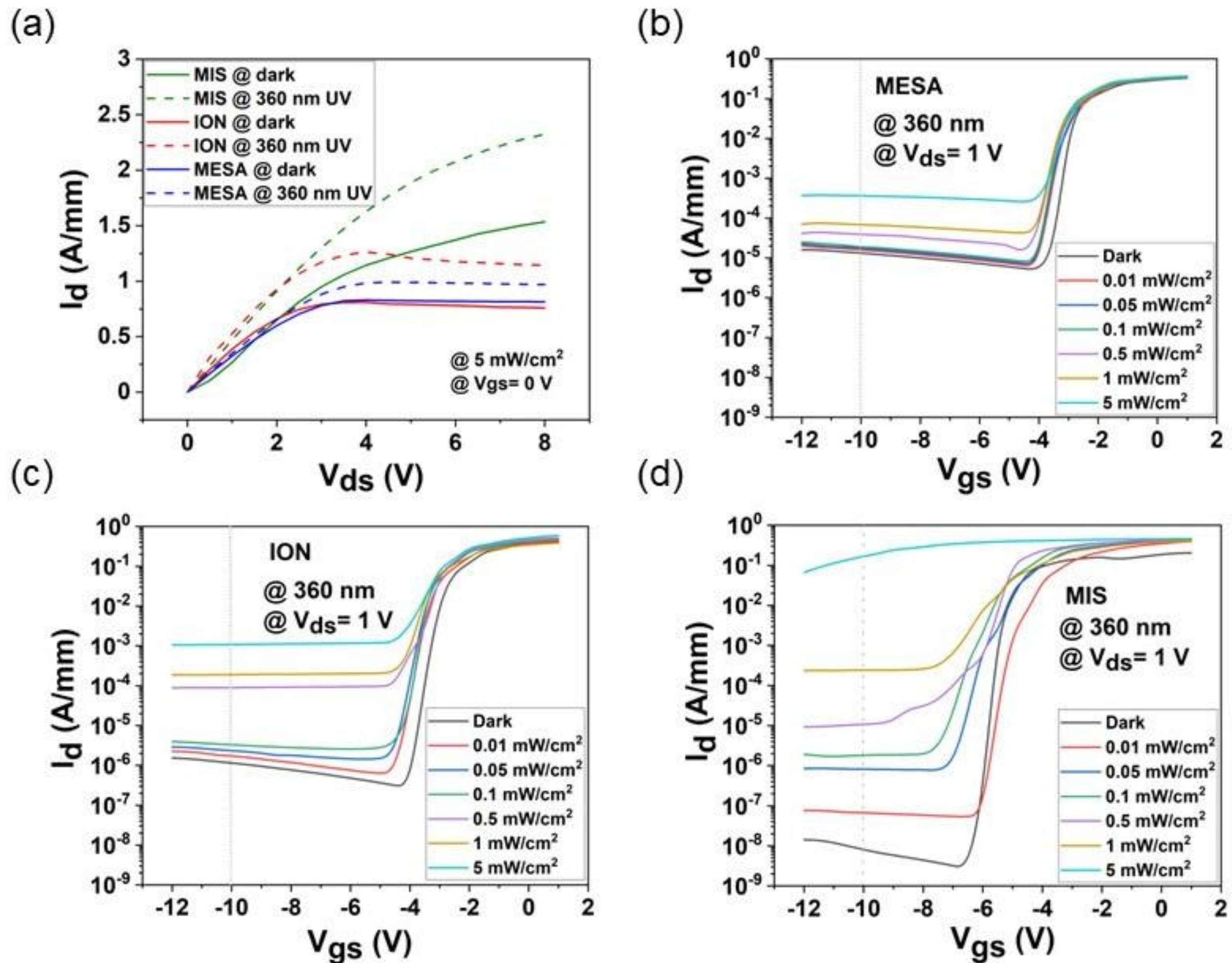

Fig 3. (a) Comparison of V_{ds}-I_d plot of different photo-HEMTs under dark and UV illumination condition. V_{gs}-I_d plots of (b) MESA, (c) ION and (d) MIS photo-HEMTs under dark condition and 360 nm UV light with various UV illumination powers.

Fig 3(a) shows the V_{ds}-I_d plot of photo-HEMTs when gate voltage is zero. The devices were measured under dark condition and UV illumination at a wavelength of 360 nm. The MIS photo-HEMT showed higher saturated drain current due to the reduction in the resistance within the source to drain region. In addition, the interface trap density was reduced due to the presence of oxide layer. This is the reason for increased sheet carrier and subsequent improvement in the saturation drain current in MIS photo-HEMT [35]. The on-state drain current (I_d) increased under UV illumination, indicating the existence of photoresponse. However, due to large on-state drain current, the dark current was quite high. To suppress the high dark current, we should operate the photo-HEMTs under off-state or depletion mode. Therefore, the photo-HEMTs were characterized under off-state condition ($V_{gs} < V_{th}$). **Fig 3(b-d)** show transfer characteristics (V_{gs}-I_d) of the devices at 360 nm with various UV illumination power densities. The threshold voltage and minimum off-state drain current of MESA photo-HEMT were measured to be around -4 V and 4.88×10^{-6} A/mm, respectively (**Fig 3(b)**). The drain current was 1.32×10^{-5} A/mm under dark condition at V_{gs}= -10V while photocurrent increased to 3.66×10^{-4} A/mm at 360 nm under the UV power density of 5 mW/cm^2. ION photo-HEMT had the threshold voltage and minimum off-state drain current of around -4 V and 2.72×10^{-7} A/mm (**Fig 3(c)**). Under the same optical power of 5 mW/cm^2, the

drain current reached to 1.09 × 10^{-3} A at V_{gs}= -10 V, leading to more than three orders of magnitude increase in ratio of photo to dark current. The threshold voltage and minimum off-state drain current of the MIS photo-HEMT were measured to be -6.5 V and 2.65 × 10^{-9} A/mm (**Fig 3(d)**). Drain current changed from 8.1 × 10^{-9} to 1.66 × 10^{-1} A/mm at V_{gs}= -10 V, indicating more than seven orders of magnitude increase under 5 mW/cm^2 UV illumination.

Photodetection mechanism

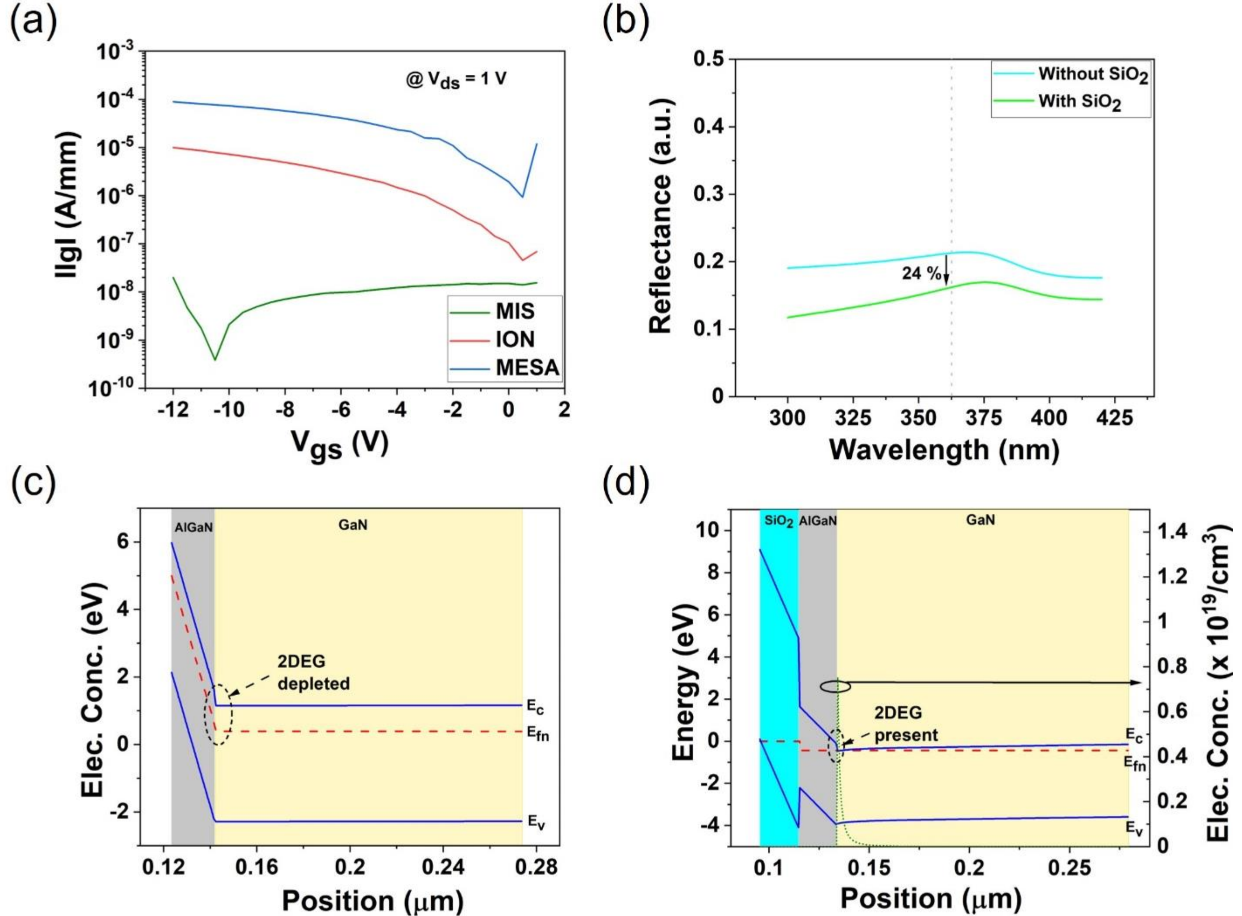

Fig 4. (a) Comparison of measured leakage current. (b) FDTD simulated reflectance spectra. (c-d) TCAD simulated band diagram of MESA and MIS HEMT structures at V_{gs} = -5 V.

We aim to understand the origin of the enhanced optoelectronic performance of MIS photo-HEMTs. When a gate bias below the threshold voltage is applied, the channel region under the gate is depleted of carriers. It results in a very low drain current under off-state as compared to on-state. Due to absorption of incident photons with energy greater than the band gap, the photo-carriers are generated, and they bridge the connection between source and drain. The photogenerated carriers are readily swept through the bridge due to presence of electric field, resulting in significantly increased off-state current. The increased off-state current (*i.e.*, photocurrent) is the evidence of light absorption in depletion mode photo-HEMTs. The off-state current under dark condition is basically the dark current. It should be as low as possible to obtain prominent photocurrent. Lower gate leakage current leads to lower off-state current in case of HEMT devices. Thus, lower gate leakage will facilitate superior photo response performance of photo-HEMT. We measured the gate leakage current under various gate voltages (**Fig 4(a)**). It clearly reveals the basis of superior photoresponse properties of MIS photo-HEMT over MESA and ION photo-HEMTs. The

gate leakage currents of the MESA, ION, and MIS photo-HEMTs were measured to be 7.28×10^{-5}, 7.18×10^{-6} and 2.10×10^{-9} A/mm, respectively, at gate voltage of -10 V. Consequently, the respective dark current of MIS and ION photo-HEMTs were four and one order of magnitude lower than that of MESA photo-HEMT. The source of gate leakage in MESA photo-HEMT arises from the carrier leakage through side wall and AlGaN barrier. The channel region of MESA photo-HEMT was defined by mesa formation and the gate contact was made around the three sides of the mesa structure. This resulted in direct contact paths between gate contact and 2DEG exposed by the mesa sidewalls.

Whereas, in case of ION photo-HEMT, the gate is only contacted on the AlGaN barrier, leading to reduced gate leakage current [36]. Meanwhile, in case of MIS photo-HEMT, an additional insulating layer exists between gate contact and channel. It refrains the carrier leakage through AlGaN barrier and mesa sidewall, resulting in the lowest gate leakage current among three types of the device configurations. Interestingly, it was observed that the photocurrent of the MIS photo-HEMT was considerably higher than those of MESA and ION photo-HEMTs. Increased photocurrent should be attributed to enhanced light trapping by SiO_2 layer [37]. To confirm this speculation, finite difference time domain (FDTD) simulation was carried out to calculate the reflectance as a function of wavelength (**Fig 4(b)**). The reflectance of SiO_2 covered channel is reduced as compared to the channel without SiO_2 in the wavelength range of 300 to 420 nm. Specifically, the degree of reflectance reduction was calculated to be around 24% at the wavelength of 360 nm. Lower reflectance leads to effective trapping of photons into channel region. Higher electric field intensity of the SiO_2 covered channel region also confirms the effective photon trapping in the channel region (**Fig S4**). In addition, SiO_2 works as a passivation layer to increase the sheet carriers in the 2DEG channel region, leading to the increased drain current.

It is also noticeable that the threshold gate voltage of MIS photo-HEMT is -6.5 V (**Fig 3(d)**) whereas it is -4 V for MESA photo-HEMT (**Fig 3(b)**). The changed threshold voltage is due to the potential drop across the 20 nm thick SiO_2. Thus, when the potential is applied to deplete the 2DEG, some potential is dropped across the dielectric and the remaining potential is consumed to deplete 2DEG. We constructed the band diagrams of MIS and MESA photo-HEMTs at V_{gs} = -5 V to understand the mechanism of the changed threshold voltage. We chose the gate bias voltage of -5 V because this bias condition makes MIS and MESA photo-HEMTs work under off-state and on-state condition, respectively. **Fig 4(c, d)** shows the band diagrams of MESA and MIS photo-HEMTs. The additional 20 nm thick insulating layer (SiO_2) drives MIS photo-HEMT to operate under on-state condition at -5 V because the 2DEG is still present with a peak electron concentration of 0.75×10^{19} /cm^3. It contributes to significant drain current. This is consistent with previously reported article [38]. However, MESA photo-HEMT operates under off-state condition at -5 V due to fully depleted 2DEG channel with negligible electron concentration.

Performance comparison of photo-HEMTs

We characterized the devices to obtain the key performance parameters (*e.g.*, responsivity (R), photo-to-dark current ratio (PDCR), detectivity (D^*), and spectral response). The biasing condition was set to be V_{gs} = -10 V and V_{ds} = 1 V unless otherwise specified. Performance parameters were extracted using the following equations [39–41],

$$R = \frac{I_{photo} - I_{dark}}{P_{\lambda}.S} \quad (1)$$

$$PDCR = \frac{I_{photo} - I_{dark}}{I_{dark}} \quad (2)$$

$$D^* = \frac{\sqrt{S}R}{\sqrt{2qI_{dark}}} \tag{3}$$

where I_{photo} and I_{dark} are the photocurrent and dark current, P_λ is the incident optical power density, S is the effective illuminated area and q is the elementary charge.

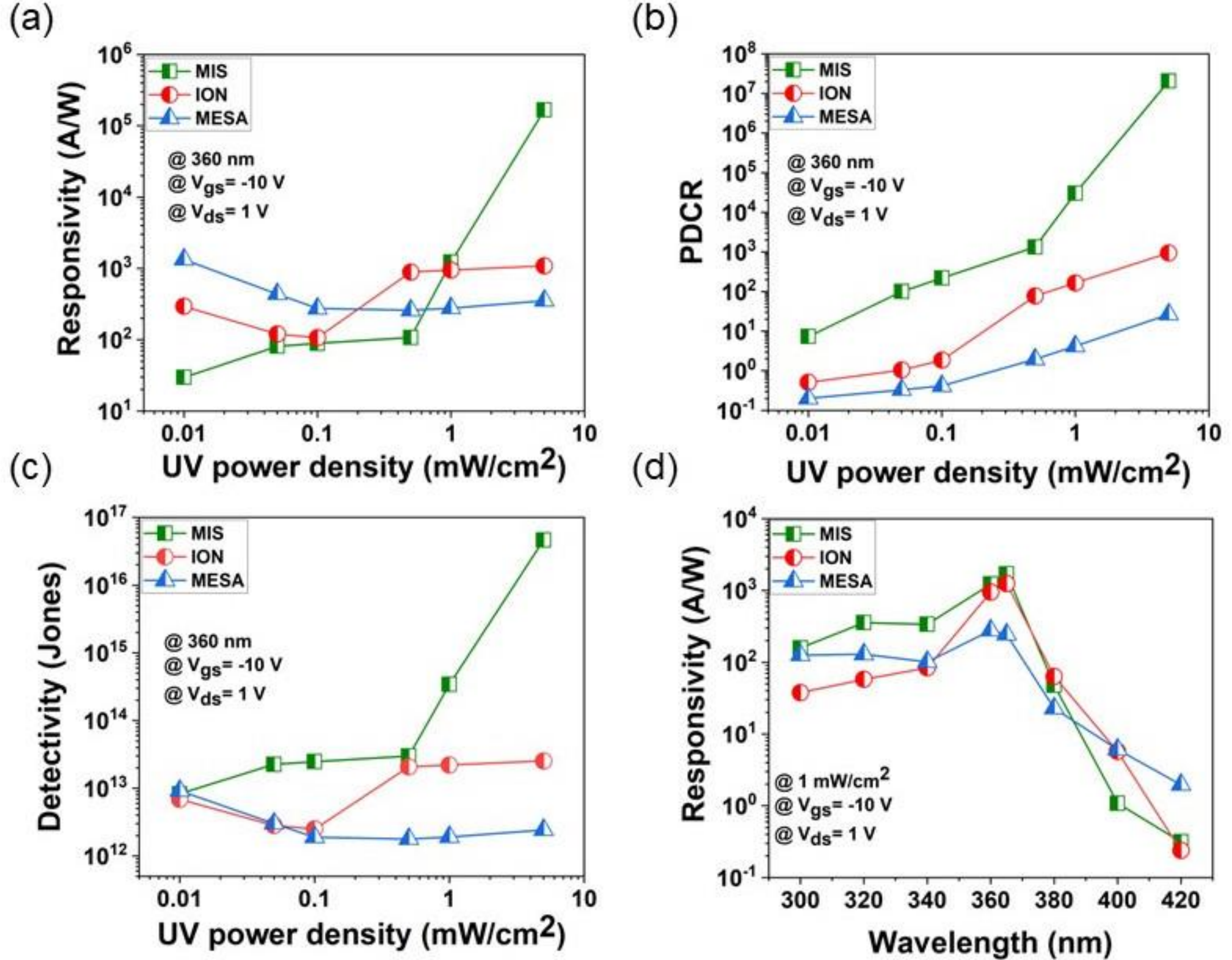

Fig 5. (a) Responsivity (b) PDCR (c) Detectivity as a function of UV power density and (d) Responsivity as a function of wavelength.

Fig 5(a) shows the power density dependence of responsivity of three types of photo-HEMTs. For lower optical power density, the responsivity of MESA photo-HEMT is the highest. However, the responsivity of MIS photo-HEMT surpasses those of MESA and ION photo-HEMTs at higher optical power density range by a considerably high margin. From the **equation (1)**, the higher photocurrent leads to higher responsivity. The photocurrent of photo-HEMT is originated from two factors: the carriers present in the channel region under off-state condition and excess carriers generated by absorbed photons. At the lower optical powers, the off-state current is the dominant contributor to photocurrent, whereas at higher optical power, the photocurrent dominantly arises from photogenerated excess carriers. As a result, the responsivity of MESA photo-HEMT is higher at lower optical power because of higher off state current. On the contrary, the responsivity of MIS HEMT at higher optical power density is much higher, indicating the existence of a high internal gain. It should be due to increase in photogenerated excess carriers arising

from photon trapping effect in presence of the SiO_2 layer. In addition, increased sheet carrier density in the 2DEG channel region should contribute to the internal gain. **Fig 5(b)** shows the PDCR at different optical power densities. MIS photo-HEMT had the highest values of PDCR throughout the optical power density range due to lower gate leakage and improved light trapping. For MIS photo-HEMTs, the responsivity and PDCR reached as high as 1.5×10^5 A/W and 2×10^7, respectively, at 360 nm.

Detectivity is another important figure of merit for PDs, which can signify its capability to detect weak light signal while rejecting noise. **Fig 5(c)** shows the detectivity as a function of optical powers. It promotes the superior detectivity of MIS photo-HEMT over other two types of photo-HEMTs. High detectivity of MIS photo-HEMT at the higher optical power is attributed to high responsivity and low dark current. The spectral responsivity measurement was carried out in the wavelength range from 300 to 420 nm (**Fig 5(d)**). The photo-HEMTs have the maximum responsivity at around 360 - 365 nm due to the band edge of GaN. The UV-Vis rejection ratio of MIS and ION photo-HEMTs between 365 and 420 nm was calculated to be 5×10^3, which is higher than that of MESA photo-HEMT.

Table 1: Performance comparison of MESA, ION, and MIS photo-HEMTs

Photo-HEMT type	**Responsivity (A/W)**	**PDCR**	**UV-Vis rejection ratio**	**Dark current (A/mm)**	**Detectivity (Jones)**	**Rise time (ms)**	**Decay time (ms)**
MESA	3.5×10^2	2.7×10^1	1.2×10^2	1.3×10^{-5}	2.4×10^{12}	102	118
ION	1×10^3	9.4×10^2	5.4×10^3	1.2×10^{-6}	2.5×10^{13}	194	212
MIS	1.5×10^5	2×10^7	5×10^3	8.1×10^{-9}	4.6×10^{16}	1235	1551

Table 1 shows the performance comparison among different types of photo-HEMTs. We also measured the transient response of the photo-HEMTs to find out their switching behaviour (**Fig S5**). An optical pulse at 360 nm with 1 mW/cm^2 was switched off and on in the interval of 10 seconds. Rise time (T_R) and decay time (T_D) are summarized in **Table 1.** It is notable that the T_R and T_D of MIS photo-HEMT is larger compared to those of MESA and ION photo-HEMTs. In case of MIS photo-HEMT, the amount of photogenerated carriers is larger than those of other two kinds of photo-HEMTs. More photogenerated carriers require prolonged time to transport through the channel region. One can observe that the rising edge of the transient response of MIS photo-HEMT clearly consists of two parts, a rapid rise followed by a slow rise until saturation. The initial fast rise is attributed to the rapid change of carrier concentration when the light is turned on. The slow rise could be due to the carrier trapping/de-trapping effects by the defects in SiO_2 layer [46]. Longer response time can be favourable for the functioning of an optical synapse [47]. **Table 2** benchmarks the performance of previously reported GaN-based three terminal phototransistors. Our MIS photo-HEMT on Si has superior UV detection properties compared to other phototransistors built on Si substrate [29], especially the dark current, which is three orders of magnitude lower. It is notable that our performance is comparable or even better than that of the photo-HEMTs on sapphire substrate. This is remarkable considering high defect densities in the films grown on Si. Although the UV-Vis rejection ratio of our device is inferior considering other three terminal GaN based phototransistors, but it performs better in comparison with previously reported photo-HEMT on Si while maintaining a very high detectivity.

Table 2: Comparison of photodetection performance among the GaN-based UV phototransistors

Device structure	Substrate	Dark current (A/mm)	Responsivity (A/W)	Detectivity (Jones)	UV-Vis rejection ratio	Reference
AlGaN/GaN HEMT	Si	3×10^{-6}	3×10^{5}	-	$\sim 10^{2}$	[42]
	Sapphire	$\sim 10^{-8}$	3×10^{6}	1.8×10^{17}	-	[40]
		$\sim 10^{-1}$	4.3×10^{7}	1.6×10^{14}	10^{3}	[33]
		4.5×10^{-1}	1.4×10^{6}	-	10^{5}	[43]
		$\sim 10^{-8}$	6.2×10^{4}	-	3.1×10^{3}	[27]
InAlN/AlGaN HEMT		6.8×10^{-8}	2.2×10^{4}	-	1.1×10^{4}	[44]
AlGaN/GaN BJT		-	5.0×10^{4}	-	$\sim 10^{8}$	[45]
GaN MOSFET		-	1.5×10^{2}	2.2×10^{13}	-	[18]
AlGaN/GaN HEMT	Si	8.1×10^{-9}	1.5×10^{5}	4.6×10^{16}	5×10^{3}	This work

Conclusion

In summary, we have demonstrated high-performance AlGaN/GaN MIS photo-HEMTs on Si substrate. The device has excellent performances such as very high responsivity (3.52×10^{2} A/W), PDCR (2×10^{7}), detectivity (4.63×10^{16} Jones), and UV-Vis rejection ratio (5×10^{3}). In addition, we also develop AlGaN/GaN photo-HEMTs by deploying Ar^{+} ion-implantation route which also gives a reasonably high responsivity, PDCR, detectivity, and UV-Vis rejection ratio of around 1×10^{3} A/W, 9.44×10^{2}, 2.53×10^{13} Jones, and 5.4×10^{3}, respectively. These two types of the photo-HEMTs have achieved higher performance than that of conventional mesa isolated AlGaN/GaN photo-HEMTs. We claim that the improvements achieved in the ION and MIS schemes are predominantly attributed to the reduction of off-state current resulted by lower gate leakage. Therefore, it is feasible to realize the advanced applications such as on-chip integration of active pixelated UV imaging systems.

Acknowledgement

This work was supported by the A*STAR, Singapore, Advanced Manufacturing and Engineering (AME) Individual Research Grant (IRG) under the Project M21K2c0107. The authors acknowledge the support of the Nanyang NanoFabrication Centre (N2FC).

Method

Fabrication of AlGaN/GaN photo-HEMTs

The fabrication process starts with the cleaning of the samples by sonicating them into the acetone, iso-propanol, and de-ionized water for 5 minutes, respectively. Device patterning at different stages of fabrication has been processed by photolithography. In case of MESA and MIS photo-HEMTs, the channel region has been defined by mesa-isolation of AlGaN/GaN. Cl_2 gas chemistry based ICP-RIE system has been deployed to achieve the mesa structure with an etching depth of above 200 nm. It reached the highly resistive carbon doped GaN buffer layer. The SiO_2 insulation in MIS photo-HEMT was deposited by PECVD. In ION photo-HEMTs, isolation of the channel region has been defined by ion-implantation based on the Ar^{+} dose and the energy of 1.1×10^{13} /cm^{2} and 45 KeV, respectively. Metal stack of Ti (20 nm)/Al (150 nm)/Ti (40 nm)/Au (60 nm) was deposited for source and drain electrodes. Rapid thermal annealing has been executed under N_2 ambient at 850 $^{\circ}$C. A thin metal stack of Ni (5 nm)/Au (5 nm) has been deposited by e-beam evaporator for gate electrodes. The schematic fabrication process flow of the three types of photo-HEMTs is shown in **Fig S6.**

Optoelectronic Measurements

Current-voltage (I-V) characteristics of the devices have been measured by Keithley 2636B source meter under dark and UV light. The UV light has been directed vertically on the devices through an optical fiber (Thorlabs; M30L02). The light source is composed of a broadband 75W Xe lamp (Horiba; LPS 100) light source attached with monochromator (PTI). The incidence of light power on the sample has been calibrated by a silicon photodetector (Thorlabs; S120VC) integrated to power meter (Thorlabs; PM100A). For transient response, the optical beam is made on/off by using a chopper (Stanford research System; SRS4).

References

[1] S. Nakamura, *Ann Phys* **2015**, *527*, 335.

[2] A.-C. Liu, P.-T. Tu, C. Langpoklakpam, Y.-W. Huang, Y.-T. Chang, A.-J. Tzou, L.-H. Hsu, C.-H. Lin, H.-C. Kuo, E. Y. Chang, *Micromachines (Basel)* **2021**, *12*, 737.

[3] F. Roccaforte, M. Leszczynski, In *Nitride Semiconductor Technology*, Wiley, **2020**, pp. 1–39.

[4] Q. Cai, H. You, H. Guo, J. Wang, B. Liu, Z. Xie, D. Chen, H. Lu, Y. Zheng, R. Zhang, *Light Sci Appl* **2021**, *10*, 94.

[5] H. Chen, K. Liu, L. Hu, A. A. Al-Ghamdi, X. Fang, *Materials Today* **2015**, *18*, 493.

[6] E. Monroy, F. Omn s, F. Calle, *Semicond Sci Technol* **2003**, *18*, R33.

[7] T. He, X. Zhang, X. Ding, C. Sun, Y. Zhao, Q. Yu, J. Ning, R. Wang, G. Yu, S. Lu, K. Zhang, X. Zhang, B. Zhang, *Adv Opt Mater* **2019**, *7*.

[8] W. Chen, X. Xu, M. Li, S. Kuang, K. H. L. Zhang, Q. Cheng, *Adv Opt Mater* **2023**, *11*.

[9] Y. Zheng, Y. Li, X. Tang, W. Wang, G. Li, *Adv Opt Mater* **2020**, *8*, 2000197.

[10] P. Wan, M. Jiang, T. Xu, Y. Liu, X. Fang, C. Kan, *Adv Opt Mater* **2022**, *10*, 2101851.

[11] J. Li, X. Xi, X. Li, S. Lin, Z. Ma, H. Xiu, L. Zhao, *Adv Opt Mater* **2020**, *8*.

[12] J. He, W. Cheng, Q. Wang, K. Cheng, H. Yu, Y. Chai, *Adv Electron Mater* **2021**, *7*, 2001045.

[13] S. J. Chang, T. M. Kuan, C. H. Ko, Y. K. Su, J. B. Webb, J. A. Bardwell, Y. Liu, H. Tang, W. J. Lin, Y. T. Cherng, W. H. Lan, *Solid State Electron* **2003**, *47*, 2023.

[14] Y. Pu, Y. C. Liang, *Appl Phys Lett* **2022**, *121*.

[15] W. Xu, Y. Shi, F. Ren, D. Zhou, L. Su, Q. Liu, L. Cheng, J. Ye, D. Chen, R. Zhang, Y. Zheng, H. Lu, *Photonics Res* **2019**, *7*, B48.

[16] O. Katz, V. Garber, B. Meyler, G. Bahir, J. Salzman, *Appl Phys Lett* **2001**, *79*, 1417.

[17] Y. Huang, D. J. Chen, H. Lu, K. X. Dong, R. Zhang, Y. D. Zheng, L. Li, Z. H. Li, *Appl Phys Lett* **2012**, *101*, 253516.

[18] H. Liu, Y. Wang, C. Liu, W. Gao, L. Han, X. Wang, J. Li, *ACS Applied Optical Materials* **2023**.

[19] Y. Pu, Y. C. Liang, *ACS Photonics* **2023**, *10*, 1293.

[20] M. Peng, Y. Liu, A. Yu, Y. Zhang, C. Liu, J. Liu, W. Wu, K. Zhang, X. Shi, J. Kou, J. Zhai, Z. L. Wang, *ACS Nano* **2016**, *10*, 1572.

[21] P. F. Satterthwaite, A. S. Yalamarthy, N. A. Scandrette, A. K. M. Newaz, D. G. Senesky, *ACS Photonics* **2018**, *5*, 4277.

[22] T.-M. Kuan, S.-J. Chang, Y.-K. Su, C.-H. Ko, J. B. Webb, J. A. Bardwell, Y. Liu, H. Tang, W.-J. Lin, Y.-T. Cherng, W.-H. Lan, *Jpn J Appl Phys* **2003**, *42*, 5563.

[23] Y.-Y. Zhang, Y.-X. Zheng, J.-Y. Lai, J.-H. Seo, K. H. Lee, C. S. Tan, S. An, S.-H. Shin, B. Son, M. Kim, *ACS Nano* **2021**, *15*, 8386.

[24] Q. Lyu, H. Jiang, K. M. Lau, *Appl Phys Lett* **2020**, *117*, 071101.

[25] H. Wang, H. You, Y. Xu, X. Sun, Y. Wang, D. Pan, J. Ye, B. Liu, D. Chen, H. Lu, R. Zhang, Y. Zheng, *ACS Photonics* **2022**, *9*, 2040.

[26] W. Wu, C. Liu, L. Han, X. Wang, J. Li, *Appl Surf Sci* **2023**, *618*, 156618.

[27] A. M. Armstrong, B. Klein, A. A. Allerman, E. A. Douglas, A. G. Baca, M. H. Crawford, G. W. Pickrell, C. A. Sanchez, *J Appl Phys* **2018**, *123*, 114502.

[28] A. Montanaro, W. Wei, D. De Fazio, U. Sassi, G. Soavi, P. Aversa, A. C. Ferrari, H. Happy, P. Legagneux, E. Pallecchi, *Nat Commun* **2021**, *12*.

[29] A. Dodda, D. Jayachandran, A. Pannone, N. Trainor, S. P. Stepanoff, M. A. Steves, S. S. Radhakrishnan, S. Bachu, C. W. Ordonez, J. R. Shallenberger, J. M. Redwing, K. L. Knappenberger, D. E. Wolfe, S. Das, *Nat Mater* **2022**, *21*, 1379.

[30] S. Arulkumaran, K. Ranjan, G. I. Ng, J. Kennedy, P. P. Murmu, T. N. Bhat, S. Tripathy, *Journal of Vacuum Science & Technology B, Nanotechnology and Microelectronics: Materials, Processing, Measurement, and Phenomena* **2016**, *34*, 042203.

[31] R. Lossy, H. Gargouri, M. Arens, J. Würfl, *Journal of Vacuum Science & Technology A: Vacuum, Surfaces, and Films* **2013**, *31*, 01A140.

[32] S.-H. Baek, G.-W. Lee, C.-Y. Cho, S.-N. Lee, *Sci Rep* **2021**, *11*, 7172.

[33] Z. H. Zaidi, P. A. Houston, *IEEE Trans Electron Devices* **2013**, *60*, 2776.

[34] S. Christiansen, M. Albrecht, H. P. Strunk, *Philosophical Magazine A: Physics of Condensed Matter, Structure, Defects and Mechanical Properties* **1998**, *77*, 1013.

[35] X. Cui, W. Cheng, Q. Hua, R. Liang, W. Hu, Z. L. Wang, *Nano Energy* **2020**, *68*.

[36] H. C. Chiu, C. H. Chen, H. L. Kao, F. T. Chien, P. K. Weng, Y. T. Gau, H. W. Chuang, *Microelectronics Reliability* **2013**, *53*, 1897.

[37] E. C. Garnett, B. Ehrler, A. Polman, E. Alarcon-Llado, *ACS Photonics* **2021**, *8*, 61.

[38] M. Miczek, C. Mizue, T. Hashizume, B. Adamowicz, *J Appl Phys* **2008**, *103*.

[39] Y. Liao, Y. Zheng, S. H. Shin, Z. J. Zhao, S. An, J. H. Seo, J. H. Jeong, M. Kim, *Adv Opt Mater* **2022**, *10*.

[40] H. Zhang, F. Liang, K. Song, C. Xing, D. Wang, H. Yu, C. Huang, Y. Sun, L. Yang, X. Zhao, H. Sun, S. Long, *Appl Phys Lett* **2021**, *118*, 242105.

[41] Y. Liao, Y. J. Kim, J. Lai, J.-H. Seo, M. Kim, *ACS Appl Mater Interfaces* **2023**, *15*, 13343.

[42] T. Narita, A. Wakejima, T. Egawa, *Jpn J Appl Phys* **2013**, *52*, 01AG06.

[43] S. H. Baek, G. W. Lee, C. Y. Cho, S. N. Lee, *Sci Rep* **2021**, *11*.

[44] L. Li, D. Hosomi, Y. Miyachi, T. Hamada, M. Miyoshi, T. Egawa, *Appl Phys Lett* **2017**, *111*, 102106.

[45] W. Yang, T. Nohava, S. Krishnankutty, R. Torreano, S. McPherson, H. Marsh, *Appl Phys Lett* **1998**, *73*, 978.

[46] B. R. Tak, V. Gupta, A. K. Kapoor, Y.-H. Chu, R. Singh, *ACS Appl Electron Mater* **2019**, *1*, 2463.

[47] Y. Mo, B. Luo, H. Dong, B. Hou, *J Mater Chem C Mater* **2022**, *10*, 13099.